npj | 2D materials and applications

Article

Published in partnership with FCT NOVA with the support of E-MRS

https://doi.org/10.1038/s41699-024-00448-x

MoS_2 decorated carbon fiber yarn hybrids for the development of freestanding flexible supercapacitors

José Tiago Carvalho[1], Afonso Correia[1], Neusmar J. A. Cordeiro[2], João Coelho[1], Sidney A. Lourenço[2,3], Elvira Fortunato[1], Rodrigo Martins[1] & Luís Pereira[1,4]

Academic and industrial efforts have focused on developing energy storage devices for wearable and portable electronics using low-cost, scalable, and sustainable materials and approaches. In this work, commercially available stretch-broken carbon fiber yarns (SBCFYs) were hybridized with mixed phases of 1 T and 2H MoS_2 nanosheets via conventional and microwave-assisted heating (CAH, MAH) without the use of binders to fabricate symmetric freestanding 1D fiber-shaped supercapacitors (FSCs). Electrochemical characterization performed in a three-electrode configuration showed promising results with specific capacitance values of 184.41 and 180.02 $F{\cdot}g^{-1}$, at 1 $mV{\cdot}s^{-1}$ for CAH and MAH, respectively. Furthermore, after performing 3000 CV cycles at 100 $mV{\cdot}s^{-1}$, the capacitance retention was 79.5% and 95.7%, respectively. Using these results as a reference, symmetric 1D FSCs were fabricated by pairing hybridized SBCFYs with MoS_2 by MAH. The devices exhibited specific capacitances of approximately 58.60 ± 3.06 $F{\cdot}g^{-1}$ at 1 $mV{\cdot}s^{-1}$ and 54.81 ± 7.34 $F{\cdot}g^{-1}$ at 0.2 $A{\cdot}g^{-1}$ with the highest power density achieved being 15.17 $W{\cdot}g^{-1}$ and energy density of $5.06{\times}10^{-4}$ $Wh{\cdot}g^{-1}$. In addition, five 1D FSCs were hand-stitched and connected in series onto a cotton fabric. These supercapacitors could power a temperature and humidity sensor for up to six minutes, demonstrating the practicality and versatility of the prepared 1D FSCs for powering future electronic systems.

Electronic textiles or e-textiles are an emerging scientific field with great potential for developing several new applications, such as smart homes[1], personal protective equipment (PPE)[2], and point-of-care systems[3]. However, these emerging wearable technologies require appropriate power supplies. Conventional supercapacitors and batteries are limited by their bulky, rigid structures and cylindrical or pouch shapes, which are not viable options when developing lightweight, durable, flexible, and comfortable wearable devices[4,5]. In this sense, fiber-based, thin, and flexible batteries and supercapacitors are emerging as suitable 1D and 2D energy storage systems to meet the power demands of wearables[6–12]. Supercapacitors have emerged as an alternative to batteries. Although they do not have the same storage energy capacity as a conventional battery, they can be charged and discharged quickly, providing high power densities. Furthermore, they have longer lifespans, enduring more charge/discharge cycles without significantly degrading their performance[13]. Carbon-based textiles (fabrics, yarns, and fibers) possess high surface area, good electrical conductivity, chemical/thermal stability, and are lightweight. They can be easily functionalized to produce 1D yarns, 2D fabrics, and 3D woven structures, serving as excellent binder-free current collectors[14,15]. Supercapacitors based on carbon-based materials can exhibit high performance, but the energy density delivered is still relatively low[16]. One of the strategies to increase their energy density is to increase the electrode's specific capacitance (C_s), which in practice can be achieved by its hybridization with nanomaterials[17]. In addition to increasing the electrode surface area, nanomaterials can promote fast and reversible Faradaic reactions from the electrode at the electrode-electrolyte interfaces, contributing to the energy storage process[18].

Molybdenum disulfide (MoS_2), a two-dimensional (2D) nanomaterial, is one of the most representative transition metal dichalcogenides (TMDs), used for energy storage and catalysis[19–22], environmental applications[23], mechanical energy harvesting[24], therapeutics, bioimaging, and biosensing[25].

[1]CENIMAT | i3N, Department of Materials Science, School of Science and Technology, NOVA University Lisbon and CEMOP/UNINOVA, Campus da Caparica, Caparica 2829-516, Portugal. [2]Laboratório de Óptica e Optoeletrônica, Departamento de Física, Universidade Estadual de Londrina (UEL), CP6001 LondrinaParaná CEP 86051-970, Brazil. [3]Laboratório de Fotônica e Materiais Nanoestruturados, Departamento de Física, Universidade Tecnológica Federal do Paraná (UTFPR), LondrinaParaná CEP 86036-370, Brazil. [4]AlmaScience, Campus da Caparica, Caparica 2829-516, Portugal. e-mail: lmnp@fct.unl.pt

MoS_2 has a layered structure similar to graphene, with S-Mo-S atoms sandwiched by van der Waals forces. It can also manifest in three different phases: the hexagonal (2H), trigonal (3R), and synthetic octahedral (1T)[21]. The large specific surface area (SSA) provided by the 2D MoS_2 nanostructure allows for rapid ion insertion/extraction within the layers, enhancing its electrochemical response[26]. Despite being a semiconductor, the 2H phase is the most stable and common form in nature and is widely considered for energy applications. Nevertheless, the advantages of the metastable 1T phase, such as its metallic character (electrical conductivity $\approx 10^5$ higher than 2H) and hydrophilicity, offer improved electron transport efficiency, reduced charge transfer resistance, and better access for ions improving the electrochemical response of the energy storage devices[27,28]. Several works[28–34] have demonstrated the potential of this 1T MoS_2 phase or a combination of 1T and 2H in supercapacitor and battery applications. However, achieving a high percentage of the 1T phase and stabilizing it is challenging as it is metastable toward heating and aging, gradually transitioning into the 2H phase[27,35]. Incorporating carbon-based conductive materials with MoS_2 has been considered an effective strategy to stabilize the 1T phase and its electrochemical activity, enhance MoS_2 stability during cycling, and ensure conductivity[6,27,36].

This work explored this hybridization by directly growing 1T and 2H MoS_2 phases by hydrothermal synthesis via conventional- and microwave-assisted heating on commercially available SIGRAFIL stretch-broken carbon fiber yarn (SBCFY). This bottom-up approach offers the advantages of producing large quantities of material with uniformity and lower production costs. Additionally, it allows MoS_2 to be grown directly into various substrates[27].

Results

Structural and morphological analysis of MoS_2 nanosheets

The hybridization of the SBCFYs with MoS_2 was carried out by hydrothermal synthesis in an oven via conventional-assisted heating (CAH) and microwave-assisted heating (MAH). Both methods have been used to synthesize numerous nanostructured nanomaterials for various energy applications[37–40]. The difference between the two mechanisms lies in the heat source and how it is distributed along the vessel. CAH has a low heating rate, resulting in a longer synthesis time and the formation of nanostructure heterogeneity due to the associated conduction and convection mechanisms. In contrast, MAH generates a uniform and homogeneous heat transfer directly to the reactants, resulting in a much faster synthesis and a more homogeneous material[40–42].

Figure 1 briefly illustrates both CAH and MAH syntheses, which were started by preparing a seed layer solution consisting of deionized water, sodium molybdate dihydrate, and thiourea (1:4). After complete dissolution, 1 m of the SBCFY was immersed in the solution for 60 min at RT and then dried in an oven at 80 °C for 60 min, Fig. 1a.

The growing solution was prepared (Fig. 1b) and placed next to SBCFY in a Teflon tube, then in an autoclave, and finally in the furnace to perform CAH. In the case of MAH, the growth solution and the SBCFY were placed in a Teflon tube and a glass vessel, respectively, and finally in the microwave. CAH was conducted at 180 °C for 12, 24, and 48 h, whereas MAH was

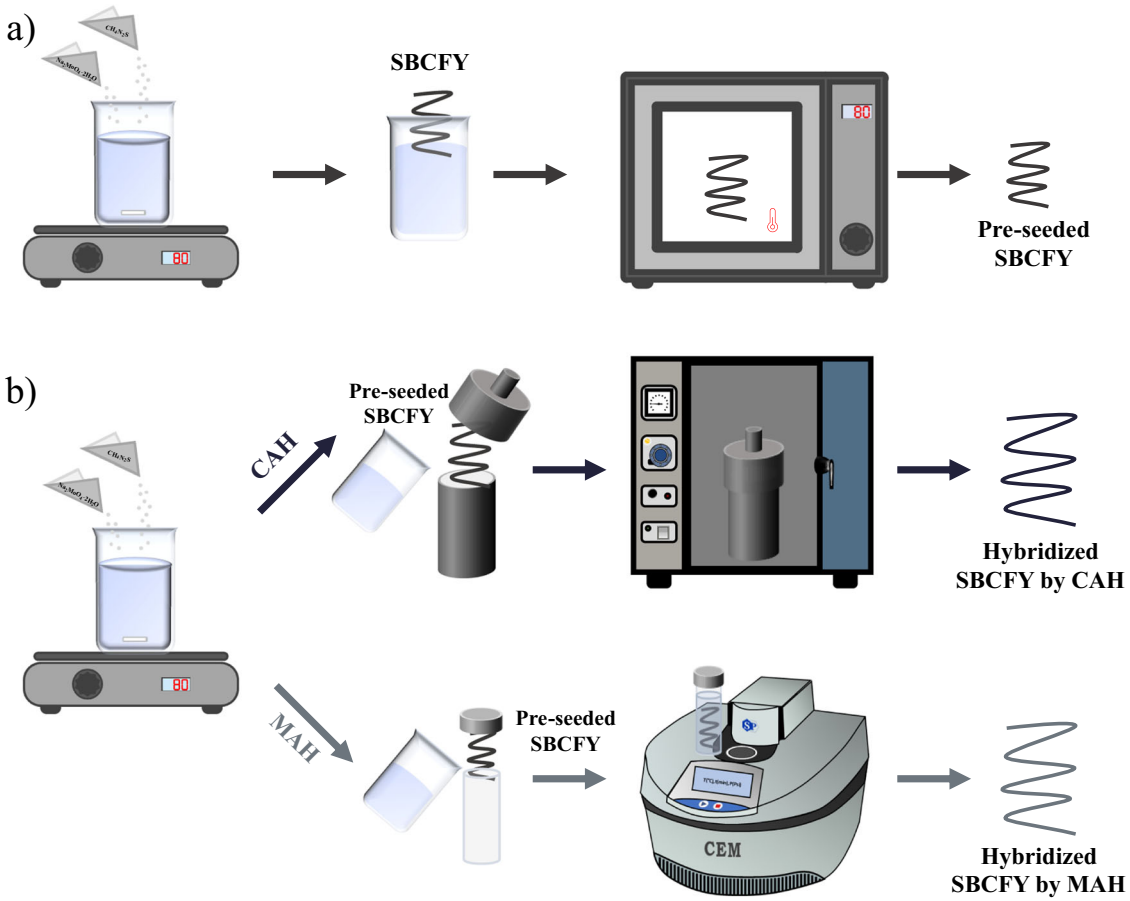

Fig. 1 | Schematic representation of the performed hydrothermal process for hybridizing SBCFY with MoS2 nanosheets. a First, the seed solution is prepared, and 1 m of SBCFY is immersed for 60 min. The SBCFY is then dried in an oven at 80 °C for 60 min and stored. **b** Next, the MoS_2 nanosheets are grown. A fresh solution is prepared and placed in an autoclave next to the pre-seeded 1 m long SBCFY. In the case of conventional assisted heating (CAH), it is transferred to the oven. For microwave-assisted heating (MAH), the solution is placed next to the 1 m SBCFY in a glass vessel and then transferred to the microwave. Finally, both hybridized SBCFYs are washed with DI and ethanol in an ultrasonic bath and stored at room temperature.

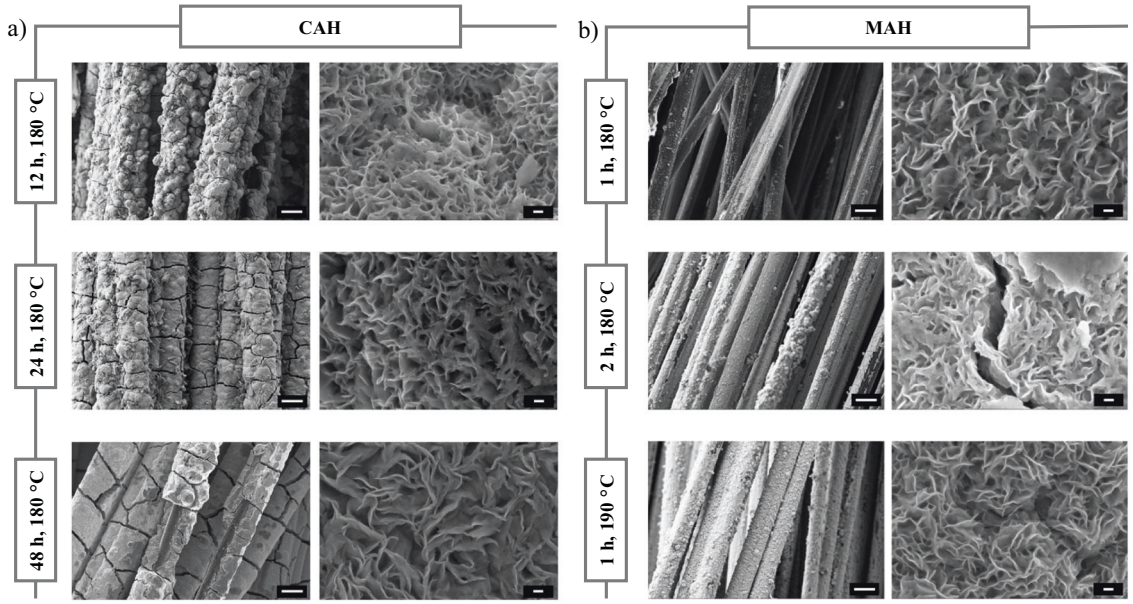

Fig. 2 | Morphology of the hybridized SBCFYs with MoS_2. Scanning electron microscopy (SEM) images of the hybridized SBCFYs with MoS_2 nanosheets grown by (**a**) conventional-assisted heating (CAH) for 12, 24, and 48 h at 180 °C (left scale: 10 µm, right scale 100 nm); and (**b**) microwave-assisted heating (MAH), for 1 and 2 h at 180 °C, and 1 h at 190 °C, respectively. (left scale: 10 µm, right scale 100 nm).

performed at 180 °C for 1 and 2 h and 190 °C for 1 h. Finally, after synthesis, the hybridized SBCFY with MoS_2 and the remaining powder were washed in an ultrasonic bath (twice in deionized (DI) water and once in ethanol) and dried and stored at RT. The morphology and uniformity of the grown MoS_2 nanostructures from both methods were examined by SEM, as shown in Fig. 2. Both methods allowed the vertical and uniform growth of 2D MoS_2 nanosheets on the SBCFYs[26,31,43,44]. As evidenced, the nanosheets, in a non-organized manner, display a high surface area, thus increasing the number of active sites for redox reactions and the size of the electric double layer (EDL). The dimension of the MoS_2 nanosheets seems insensitive to the growth conditions used in MAH, while the same does not happen for CAH, where the nanoplates at the surface of the electrodes tend to become larger as the synthesis time increases, which is detrimental in terms of effective surface area and mechanical stability when ions are intercalated. Another relevant difference is the control over the growth process when using MAH, and, thus, over the MoS_2 mass grown on top of SBCFYs. CAH results in more MoS_2 mass than MAH, as confirmed by the difference in the thickness layer (Fig. 2) and the SBCFYs' weights after synthesis (Supplementary Table 1). As the CAH synthesis time increases from 12 to 48 h at the same temperature of 180 °C, more uniform and homogeneous coverage of the SBCFY is achieved. However, the amount of formed material leads to cracking, which may cause the MoS_2 nanosheets to detach from the yarn. Furthermore, the thicker the layer of active material, the greater the resistance[45]. On the other hand, and due to the mechanism involved, MAH synthesis is less time-consuming; after 2 h at 180 °C, a uniform and homogeneous hybridization of 2D MoS_2 nanostructures on SBCFY is achieved. This led us to choose the synthesis of CAH performed at 180 °C for 12 h and MAH at 180 °C for 2 h. The direct growth of SBCFYs and their nanostructuring with MoS_2 avoids using binders, which affect conductivity and adhesion, and allows a uniform growth of the nanostructures along the yarn with an improved surface area, shortening the ion diffusion path[26,36,43].

Figure 3a shows the XRD diffractograms for as-synthesized samples from CAH and MAH, for 12 h and 2 h, at 180 °C, respectively. The diffractograms for SBCFYs and MoS_2 powder remaining from the synthesis are also presented. The standard JCPDS card 37–1492 was also included to facilitate the identification of the 2H MoS_2 phase. Compared to bulk 2H MoS_2 (JCPDS card 37–1492), the peaks found at 33° and 58° correspond to the (100) and (110) planes, respectively. However, the same data do not correspond to the (002) plane located at 14.4°. However, it is possible to note the appearance of two peaks, one at 9.03° and 9.2° for both syntheses and another at 18.65° for the CAH synthesis. These two peaks are usually attributed to the intercalation of molecules and ions between the MoS_2 layers[19,46,47]. Using Bragg´s law, the interlayer distance for the peaks at 9.03° and 9.2° is 0.979 and 0.960 nm for CAH and MAH, respectively. The peak at 18.65° also has an interlayer distance of 0.475 nm. This confirms the expansion of the interlayer since the reference plane interlayer distance of 2H MoS_2 (002) is 0.62 nm[46]. However, as reported, this interlayer expansion should not be direct evidence for forming the 1T-MoS_2 phase[19]. Other reports claim that the shift or appearance of these two peaks is the formation of the 1T-phase due to the intercalation of ammonium ions[48,49]. The metallic 1T-phase could also be identified by the appearance of a peak before 10°, around 7.3°, which would correspond to the (001) plane of the MoS_2[20].

Raman and XPS measurements were also conducted to investigate whether the metallic 1T-MoS_2 phase was synthesized. Figure 3b shows the Raman shift performed for both synthesis methods, with the vibrational modes corresponding to the 1T (J_1, J_2, and J_3) and 2H-phase (E^1_{2g} and A^1_g) also marked. The Raman analysis of the fresh sample corresponding to the CAH method shows all the modes related to the metallic 1 T and semiconducting 2H phases. The same does not happen in the sample corresponding to the MAH method, which could be related to the analyzed region of the SBCFY. Interestingly, the same set of samples exhibited both phases after 15 days, as shown in Supplementary Fig. 1. As mentioned, the 1T phase is metastable to aging, heating, and laser irradiation. For this purpose, a detailed aging analysis was performed at RT in air and N_2 storage conditions, as shown in Supplementary Fig. 1. After 15 days, both the CAH synthesis carried out for 12 h at 180 °C and the MAH synthesis carried out for 2 h at 180 °C show the vibrational modes associated with the metallic phase. However, this does not happen after 60 days, indicating its metastable nature. Furthermore, the fact that the laser power can induce the in-situ phase transformation should not be ignored[20], where the thinner MoS_2 layer tend to be more sensitive.

As shown in Fig. 3c–f), the XPS spectra reveal three distinct peaks in the Mo 3d region and two in the S2p region. In the Mo 3d region, one pair with binding energies of 228.4 eV and 231.5 eV corresponds to the Mo^{4+} $3d_{5/2}$ and $3d_{3/2}$ of the 1T-MoS_2 phase. Another pair at 230.2 eV and 233.3 eV corresponds to the Mo^{4+} $3d_{5/2}$ and $3d_{3/2}$ of the 2H-MoS_2 phase. The last pair

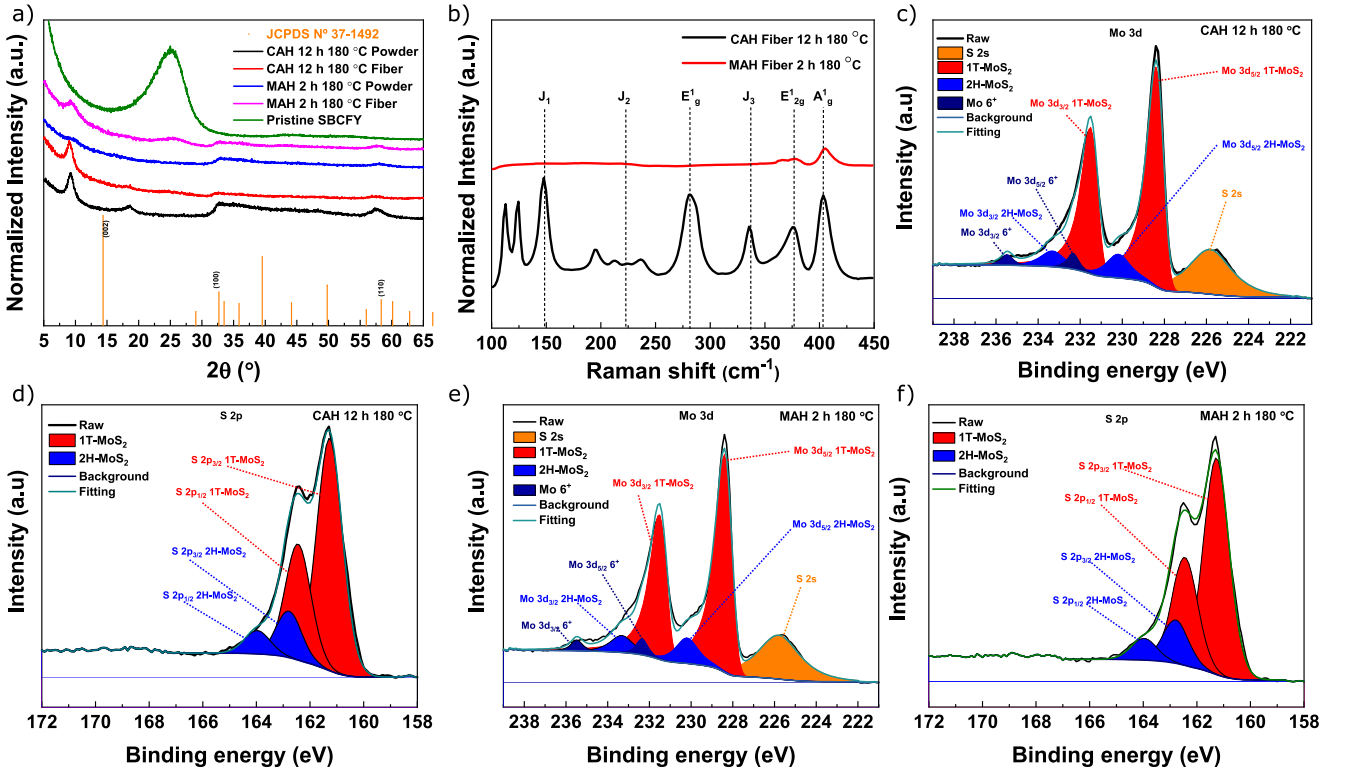

Fig. 3 | Structural characterization of hybridized SBCFYs with MoS_2. a The XRD diffractograms of the hybridized SBCFYs with MoS_2 by CAH and MAH, for 12 and 2 h, at 180 °C, respectively, as well as (**b**) the Raman spectra, and the respective XPS spectra of (**c**) Mo3d CAH, (**d**) S2p CAH, (**e**) Mo3d MAH, (**f**) S2p MAH.

located at 232.4 eV and 235.5 eV, corresponding to the Mo^{6+} $3d_{5/2}$ and $3d_{3/2}$, suggests the presence of Mo-O bonding, i.e., the presence of Molybdenum Oxide and/or partial oxidation of MoS_2[20,26,33]. The band at 225.9 eV corresponds to the S 2 s region, confirming the Mo-S bond[26]. Similarly, the analysis of the S 2p region of the spectra revealed two pairs of bands. One pair with bands at 161.3 eV and 162.5 eV, corresponding to the $2p_{3/2}$ and $2p_{1/2}$ of 1T-MoS_2, and another pair with bands at 162.8 eV and 164 eV corresponding to the $2p_{3/2}$ and $2p_{1/2}$ of 2H-MoS_2[30]. This detailed analysis confirms that the SBCFYs were successfully hybridized with a mixed phase of 1T and 2H MoS_2 nanosheets. The known features of the 1T phase, such as higher conductivity and hydrophilicity, are expected to improve the electron transport efficiency and thus enhance the electrochemical response[27,28].

Three-electrode electrochemical characterization

Electrochemical characterization, including cyclic voltammetry (CV), galvanostatic charge-discharge (GCD), and electrochemical impedance spectroscopy (EIS), was performed on both samples synthesized by CAH at 180 °C for 12 h and MAH at 180 °C for 2 h. The hybridized SBCFYs with MoS_2 nanosheets were laminated between thermal laminating pouches, as illustrated in Fig. 4a, leaving only 1 cm of its length accessible for electrochemical processes.

Figure 4c,d shows the CV curves obtained in a three-electrode configuration for the hybridized SBCFY with MoS_2 nanosheets by CAH and MAH, respectively. Both exhibit a voltage window of 1 V, with no redox peaks, and the quasi-rectangular shape predominates at low scan rates (1 to 20 $mV{\cdot}s^{-1}$), indicating the good capacitive behavior of the electrodes[20]. The contribution of pristine SBCFY is minimal compared to hybridized SBCFYs by both hydrothermal routes as shown in Supplementary Fig. 2. As the scan rate increases, the CVs deviate from the quasi-rectangular shape. In addition, the respective GCD curves (Fig. 4e, f) show a quasi-symmetric triangular shape, indicating EDL formation and possibly pseudocapacitance, resulting from fast and reversible redox reactions when ions from the electrolyte are electrochemically adsorbed on or near the surface of the MoS_2 nanosheets[13,26]. The variation of the specific capacitance (C_s) considering four samples from both syntheses at different scan rates and current densities is shown in Fig. 4g, h. From the CVs, the highest achieved C_s for CAH and MAH were 184.41 $F{\cdot}g^{-1}$ and 180.02 $F{\cdot}g^{-1}$, respectively, at 1 $mV{\cdot}s^{-1}$. The C_s obtained from the GCD for CAH was 189.02 $F{\cdot}g^{-1}$, while for MAH was 193.02 $F{\cdot}g^{-1}$, at 0.5 $A{\cdot}g^{-1}$. It is also possible to validate the reproducibility of the hybridized SBCFYs with MoS_2 obtained from both syntheses.

The Dunn method was used to estimate the contribution of capacitive and diffusion-controlled processes in the storage mechanism[13,29] The diffusion-controlled mechanism predominates for both types of electrodes at low scan rates (1 to 20 $mV{\cdot}s^{-1}$), Supplementary Fig. 3. These mechanisms are associated with fast and reversible faradaic redox reactions that can occur, allowing charge transfer and the diffusion of ions within the MoS_2. As the scan rate increases, there is less time for these reactions to occur, and capacitively controlled mechanisms become dominant. EDL formation and pseudocapacitance (near surface adsorption) are predominant in this regime. Supplementary Fig. 4 shows the Bode plot for both syntheses, demonstrating that the capacitive region is reached at low frequencies, namely 0.1 and 0.25 Hz, for CAH and MAH, respectively. From the Nyquist plot at 1 kHz, the ESR was determined to be 18.48 Ω for the CAH electrode and 16.24 Ω for the MAH electrode. The cycling stability of both electrode types was tested by performing 3000 CV cycles at 100 $mV{\cdot}s^{-1}$. The CAH electrode has a capacitance retention of 79.5%, while the MAH electrode retains 95.7%, as shown in Fig. 4i,j. The CAH shows a significant capacitance loss in the first 200 cycles. However, although MAH-related electrodes show a similar capacitance loss in the first 200 cycles, there is a recovery during the following cycles, which could be related to the stabilization of the MoS_2 in the presence of the 1 M Na_2SO_4 aqueous electrolyte[50]. After 3000 cycles, MoS_2 nanosheets are absent in some fibers of the SBCFY where CAH was used (Fig. 4k), which may explain the decrease in capacitance retention over cycling. Considering that CAH may result in a more fragile hybridization, the cycling stability tests may lead to the subsequent detachment of the MoS_2 from the multiple carbon fibers.

However, SBCFY hybridized with MAH (Fig. 4l) still shows the presence of MoS_2 nanostructures. EIS characterization was conducted before

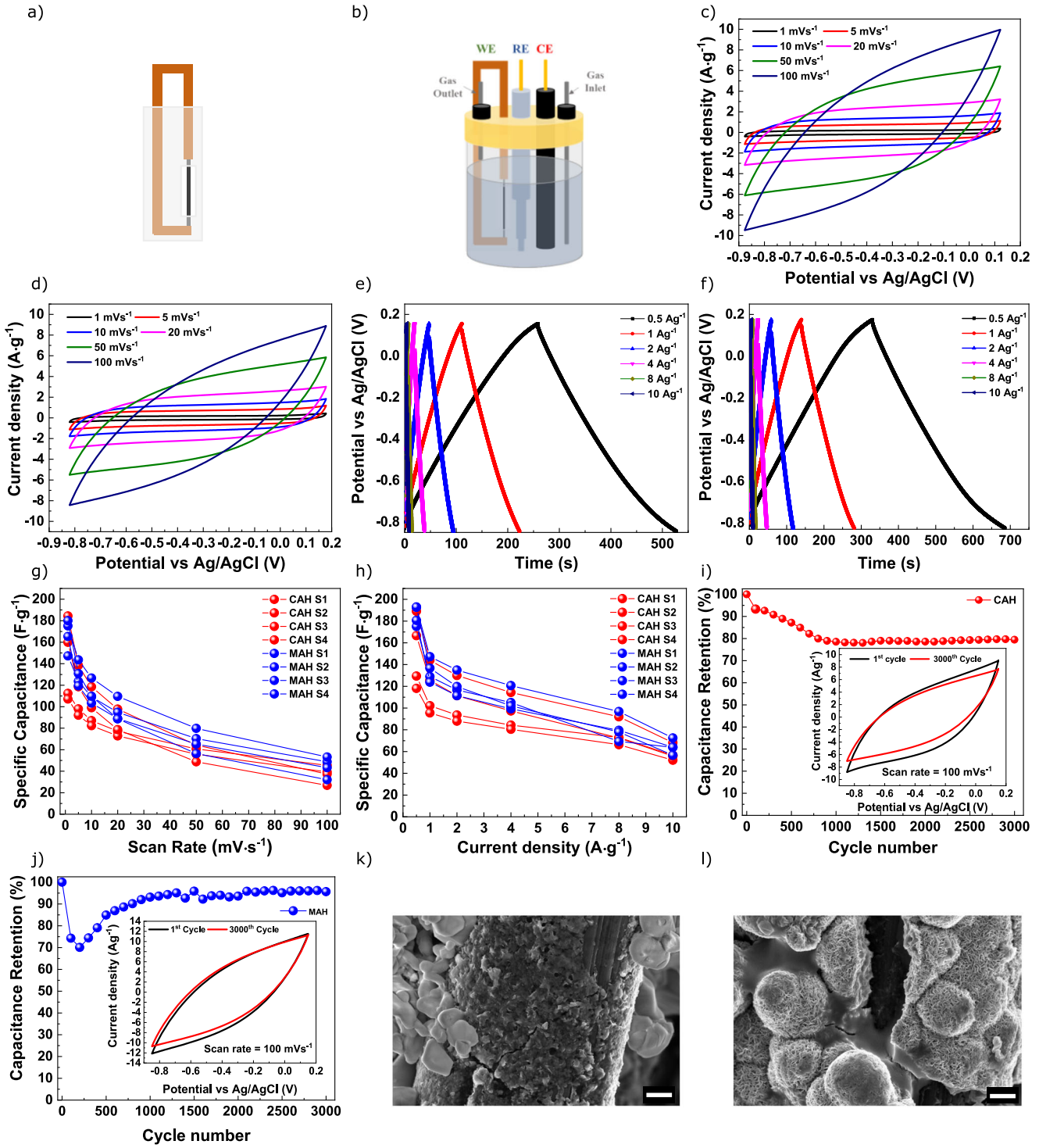

Fig. 4 | Electrochemical characterization in three-electrode configuration. Schematic representation of the electrochemical characterization setup, where (**a**) the SBCFY/MoS_2 is laminated between thermal laminating pouches and conductive copper tape for access, and (**b**) it is assembled in a three-electrode configuration in an electrochemical cell, using Ag/AgCl as the reference electrode (RE) and graphite rod as the counter electrode (CE). CV curves of a single SBCFY/ MoS_2 electrode by (**c**) CAH and (**d**) by MAH, in a three-electrode configuration, and the corresponding (**e**) and (**f**) GCD curves. The specific capacitance variation of four electrodes synthesized by CAH and MAH (**g**) at different scan rates, ranging from 1 to 100 $mV{\cdot}s^{-1}$ and (**h**) at different current densities, ranging from 0.5 to 10 $A{\cdot}g^{-1}$, respectively. The cycling performance, at a scan rate of 100 $mV{\cdot}s^{-1}$ for 3000 cycles in a potential window of 1 V corresponding to **i**) CAH and **j**) MAH, and the respective (**k**, **l**) SEM images of the electrodes after cycling. Scale:10 μm.

and after the 3000 CV cycles, and the results are shown in Supplementary Fig. 5. The Bode plot for both syntheses shows that the capacitive region is reached at a lower frequency after the 3000 CV cycles, changing from 0.16 to 0.05 Hz and from 0.08 to 0.05 Hz for CAH and MAH, respectively. The Nyquist plot shows a change in ESR with an increase from 17 Ω to 22.33 Ω for CAH and a decrease from 45.61 Ω to 37.7 Ω for MAH. It is worth noting that this is a freestanding electrode, characterized using a three-electrode configuration, as displayed in Fig. 4a, in an aqueous electrolyte. Therefore, we should not underestimate the resistances associated with the connections between the hybridized SBCFYs with the copper tape and the connection to

the potentiostat. This may help explain the differences in the initial ESRs at 1 kHz for both hybridized electrodes SBCFYs before the cycling tests.

Electrochemical characterization of 1D FSCs

To demonstrate the practical application of the hybridized SBCFYs with MoS_2 nanosheets, an additional MAH synthesis was performed at 180 °C for 2 h. Symmetric 1D FSCs, Fig. 5a, were fabricated by dipping each single electrode five times in the PVA/H_3PO_4 gel electrolyte and allowing them to dry at room temperature for 20 min between each dipping. The separator, consisting of a Whatman™ lens cleaning tissue 105, was wrapped around one of the electrodes before the assembly was immersed in the PVA/H_3PO_4 electrolyte for 5 min. The two electrodes were placed side by side and then the ends and center were tied together with a cotton thread. Finally, the assembly was dipped back into the electrolyte and held together with the aid of a dryer. The active length of the fabricated 1D FSCs was 2.5 cm.

Figure 5b shows the electrochemical characterization of the fabricated 1D FSCs, where SBCFYs were hybridized with MoS_2 by MAH. As expected, the capacitive domain is preserved within the stable voltage window of 0.8 V up to 100 mV·s^{-1}. The C_s was determined for the four devices considering the different scan rates and current densities, Fig. 5d, e. The highest average C_s was 58.60 at 1 mV·s^{-1} and 54.81 at 0.2 A·g^{-1}, with a standard deviation of 3.06 F·g^{-1} and 7.34 F·g^{-1}, respectively. The confirmed discrepancy between the four 1D FSCs is attributed to the handmade manufacturing process, including the different gel states and drying conditions of the PVA/H_3PO_4 gel electrolyte and the distance between the two hybridized SBCFYs electrodes. The rapid evaporation of water from PVA hydrogels can significantly reduce their ionic conductivity. After solidification, the PVA-based electrolytes become rigid, and the rapid self-discharge affects the performance of the devices[51]. These issues may affect the 1D FSCs and explain the observed variations. This section considers factors that could influence the performance of 1D FSCs, and which may account for the observed variations. The energy and power characteristics of the devices are shown in the Ragone plot (Fig. 5f). The highest power density achieved was 15.17 W·g^{-1}, while the energy density was 5.06×10^{-4} Wh·g^{-1}.

The Supplementary Table 2 compares the performance of single hybridized SBCFYs with MoS_2 and the relevant literature. It is essential to exercise caution when making cross-comparisons since the measurement set-ups, metrics, and device dimensions, active material mass, among other factors, can significantly vary across the different reports. Regarding electrochemical performance, the MoS_2 hybridized SBCFYs electrodes produced in this work exhibit a higher operational potential window, i.e., 1 V and specific capacitances of 189.02 F·g^{-1} and 193.02 F·g^{-1} at 0.5 A·g^{-1}, respectively. Moreover, both MoS_2 synthesis methods resulted in high capacitance retention, 79.5%, and 95.7%, after 3000 CV cycles, the last surpassing several reported systems. Finally, another advantage over other works is the demonstration that the MAH enables the functionalization of long SBCFYs (1 meter long) with high-performing MoS_2 in a much shorter time than the conventional hydrothermal route.

As shown in Fig. 5g, five 1D FSCs were stitched onto cotton fabric and connected in series using copper tape and silver yarn. The arrangement successfully powered a temperature and humidity sensor (Fig. 5h) up to 6 min, as presented in Fig. 5i, showcasing its potential application as a future power source for wearable applications.

Discussion

We have successfully hybridized commercially available SBCFYs with MoS_2 nanosheets via hydrothermal synthesis through conventional- and microwave-assisted heating. Both methods allowed the uniform growth of metallic 1T and semiconducting 2H MoS_2 phases. However, via MAH was possible to hybridize the SBCFYs in 2 h at 180 °C compared to the 12 h required via CAH. The resulting MoS_2 nanosheets provide an increase in surface area and enhancement of the device's electrochemical performance. The CVs yielded the highest specific capacity of 184.41 and 180.02 F·g^{-1}, for CAH and MAH, respectively, at 1 mV·s^{-1}. Using the GCD for estimation, the values obtained are 189.02 and 193.02 F·g^{-1}, for CAH and MAH, respectively at 0.5 A·g^{-1}. The MAH method used in this work also represents a time-effective and cost-effective process for synthesizing flexible free-standing supercapacitors. We have shown that microwave-assisted growth enables the production of high-performing MoS_2 in a much shorter time than the conventional hydrothermal route. Long carbon fiber yarns (1 meter long) were fully functionalized demonstrating that the materials and methods used in this work can upscale. The potentiality of the fabricated 1D FSCs was demonstrated by powering a humidity and temperature sensor for six minutes. This was achieved by stitching five devices in series onto a cotton fabric, showcasing the potential of textile-based electrochemical energy storage devices for powering wearable electronics.

Methods

Materials and chemicals

Thiourea (CH_4N_2S CAS:62-56-6) from MERCK, sodium molybdate dihydrate ($Na_2MoO_4{\cdot}2H_2O$ CAS:10102-40-6) from PanReac Applichem, deionized water (Millipore), sodium sulfate (Na_2SO_4) from PanReac Applichem, Poly(vinyl alcohol) (PVA, Sigma-Aldrich, $M_w \approx 61000$); Phosphoric Acid (H_3PO_4, Fluka, ≥ 85%); SIGRAFIL stretch-broken carbon fiber yarn (SBCFY) C SB70-3.3/240-R100 70 (2×35) tex from SGL Group The Carbon Company and lens cleaning tissue 105 (Whatman™).

Direct growth of MoS_2 nanosheets on SBCFY by hydrothermal synthesis

The direct growth of MoS_2 nanosheets on the SBCFY was carried out by hydrothermal synthesis via conventional-assisted heating (CAH), using an oven, and microwave-assisted heating (MAH). The procedure was adapted from a previously published work[46]. As a starting point, a seed layer solution was prepared by mixing deionized water, sodium molybdate dihydrate, and thiourea (1:4). Next, 1 meter of SBCFY was immersed in the solution for 60 min at room temperature. The SBCFY was then dried in an oven at 80 °C for 60 min before being transferred to a fresh solution with the same molar ratio for both the CAH and MAH hydrothermal methods.

CAH was carried out for 12, 24, and 48 h at 180 °C, using an autoclave and a Teflon tube filled with the solution and the SBCFY placed inside the Nabertherm furnace. For MAH, the Teflon tube was placed inside a glass vial and heated using a CEM Discovery SP microwave synthesizer at 100 W for different temperatures and times: 180 °C for 1 and 2 h and 190 °C for 1 h. After both syntheses, the products were removed and cooled to room temperature. The SBCFYs were removed from the Teflon tubes, washed in ultrasonic baths (twice in deionized (DI) water and once in ethanol, 5 min each), and dried and stored in a clean container. The loading amounts of MoS_2 in the SBCFYs were determined by comparing the weights of the SBCFYs before and after synthesis using a Mettler Toledo AT21 Comparator microscale.

Preparation of PVA H_3PO_4 electrolyte solution

The PVA/H_3PO_4 electrolyte solution was prepared by mixing 3 g of PVA in 30 mL of deionized water and heated to 80 °C under stirring until the solution became clear. Subsequently, 1.5 mL of H_3PO_4 was carefully added to the previous solution and allowed to reach room temperature under stirring before being used.

Fabrication of fiber-shaped supercapacitors

Flexible and symmetric 1D FSCs were fabricated with a planar configuration, using commercially available SBCFYs electrodes hybridized with MoS_2, by MAH, with an active length of 2.5 cm. Every single electrode was dipped 5 times in the PVA/H_3PO_4 electrolyte solution and dried for 20 min, at room temperature, between each dip. After that, lens cleaning tissue 105, from Whatman™ was wrapped, as the separator, around one of the electrodes and immersed for more than 5 min in the electrolyte. Finally, both electrodes were placed symmetrically and tied together with a cotton thread at the ends and center. The assembly was then immersed in the PVA/H_3PO_4 electrolyte and dried with a hairdryer.

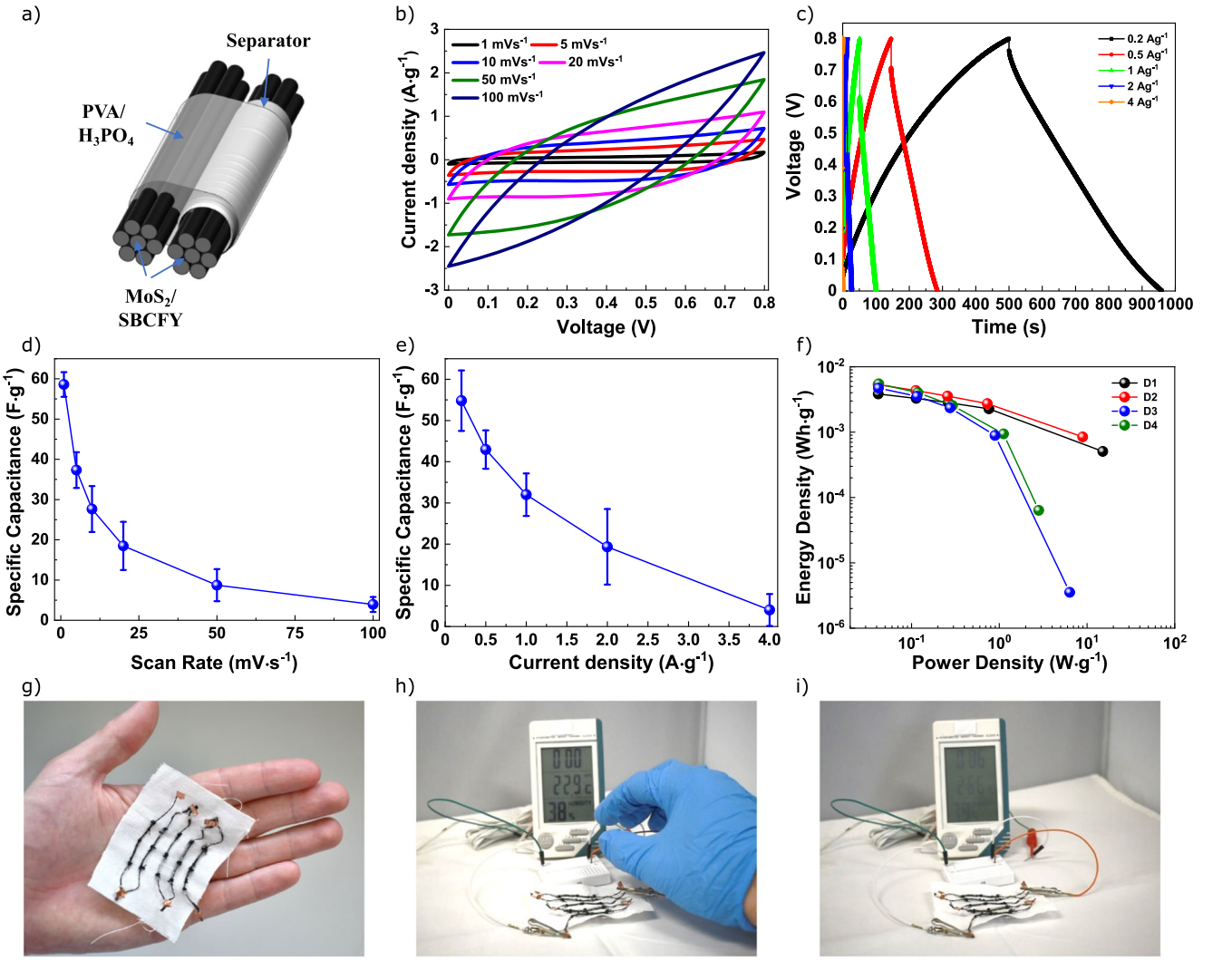

Fig. 5 | Electrochemical characterization in two-electrode configuration. **a** Schematic representation of the symmetric 1D FSCs, SBCFYs hybridized with MoS_2 by MAH, **b** CV curves of a single 1D FSCs MoS_2, **c** the corresponding GCD curves, at different current densities, ranging from 0.2 to 4 A·g^{-1}. The average specific capacitance of four 1D FSCs, **d** at different scan rates, ranging from 1 to 100 mV·s^{-1}, and **e** at different current densities, ranging from 0.2 to 4 A·g^{-1}, respectively. The error bars represent the standard variation. **f** The Ragone plot of four 1D FSCs. **g** The photograph of five devices sewn on a cotton fabric and connected in series and **h** the photograph of a humidity and temperature sensor being powered by them, **i**) up to 6 min.

Characterization

X-ray diffraction (XRD) analysis was employed to determine the crystallinity of the synthesized MoS_2 and detect the various phases. The measurements were performed using an X-ray diffractometer (PANAlytical Xpert PRO MRD) in a 2θ range from 5° to 65°. Raman spectroscopy was additionally utilized to confirm the presence of the different MoS_2 phases. Raman measurements were conducted using an air-cooled charge-coupled device (CCD) and a He–Ne laser operating at 50 mW of 532 nm laser excitation in a Renishaw inVia Qontor micro-Raman spectrometer. The spectral resolution of the spectrometer is 0.3 cm^{-1}. The laser beam was focused with a 100× Leica objective lens (N Plan EPI) with a numerical aperture of 0.85. An integration time of 10 scans of 20 s each was used for all measurements to reduce the random background noise produced by the detector without any significant effect on the acquisition time. The laser intensity was set to 5 mW. Additionally, the triplicates were taken from all spectra. Structural and morphological analyses of the MoS_2 hybridized SBCFYs hybridized with MoS_2 were conducted using SEM-FIB at a Carl Zeiss AURIGA CrossBeam workstation with an acceleration voltage of 5 kV and an aperture size of 30 µm. The samples' chemical and phase composition analysis was performed using an X-ray and Ultraviolet Photoelectron Spectroscopy (XPS/UPS) Kratos Axis Supra. Measurements were made with monochromatized (1486.6 eV) A1 Kα X-Ray at a power of 22 5 W. The analyzer's pass energy was 20 eV for detailed scans and 160 eV for wide scans. The spectra were fitted using the CasaXPS software by Casa Software Ltd.

Electrochemical characterization

The electrochemical characterization of the SBFCYs hybridized with MoS_2 and the 1D FSCs was carried out using Gamry Instruments Reference 600 potentiostat. A three-electrode configuration (BEC from redoxme) was used with a silver/silver chloride reference electrode (RE) (Ag/AgCl from redoxme), a graphite rod (GR 6/70 mm from redoxme) as the counter electrode (CE). At the same time, SBCFYs were hybridized with MoS_2 and tested as the working electrode (WE). Before mounting the assembly in the potentiostat, the electrochemical cell was filled with 25 mL of 1 M Na_2SO_4 aqueous electrolyte and purged with nitrogen for 30 min. The WE was fabricated by cutting the original yarn into 2 cm segments and laminating them in polymeric foils, with copper tape attached to the ends of the fiber to act as the current collector. Only 1 cm of the WE was available for electrochemical characterization.

Cyclic voltammetry (CV) was performed in a 1 V potential window for scan rates of 1, 5, 10, 20, 50, and 100 mV·s^{-1}. Electrochemical

impedance spectroscopy (EIS) was performed at open circuit potential (OCP) in a frequency range from 10 mHz to 100 kHz, at 5 mV AC voltage amplitude. Galvanostatic charge-discharge (GCD) was performed in chronopotentiometry mode at current densities of 0.5, 1, 2, 4, 8, 10 $A{\cdot}g^{-1}$. CVs were done for 3000 cycles at 100 $mV{\cdot}s^{-1}$for cycling tests. An EIS was done before the first cycle and after the 3 000 cycles, in a frequency range of 10 mHz to 10 kHz, at 5 mV AC voltage amplitude. A two-electrode configuration was used for the electrochemical characterization of the 1D FSCs, using PVA/H_3PO_4 as the electrolyte. CV and GCD were conducted within a 0.8 V voltage window, using the same scan rates and current densities of 0.2, 0.5, 1, 2, and 4 $A{\cdot}g^{-1}$, respectively.

Data availability

All data generated or analysed during this study are included in this published article (and its supplementary information files).

Received: 22 July 2023; Accepted: 6 February 2024;
Published online: 12 March 2024

References

1. Choi, H. W. et al. Smart textile lighting/display system with multifunctional fibre devices for large scale smart home and IoT applications. *Nat. Commun.* **13**, 814 (2022).
2. Basodan, R. A. M., Park, B. & Chung, H.-J. Smart personal protective equipment (PPE): current PPE needs, opportunities for nanotechnology and e-textiles. *Flex. Print. Electron.* **6**, 043004 (2021).
3. Chen, G. et al. Electronic Textiles for Wearable Point-of-Care Systems. *Chem. Rev.* **122**, 3259–3291 (2022).
4. Jost, K., Dion, G. & Gogotsi, Y. Textile energy storage in perspective. *J. Mater. Chem. A* **2**, 10776 (2014).
5. Sundriyal, P. & Bhattacharya, S. Textile-based supercapacitors for flexible and wearable electronic applications. *Sci. Rep.* **10**, 1–15 (2020).
6. Liao, M., Ye, L., Zhang, Y., Chen, T. & Peng, H. The Recent Advance in Fiber-Shaped Energy Storage Devices. *Adv. Electron. Mater.* **5**, 1800456 (2019).
7. Kong, L., Tang, C., Peng, H., Huang, J. & Zhang, Q. Advanced energy materials for flexible batteries in energy storage: A review. *SmartMat* **1**, 1–35 (2020).
8. Choudhry, N. A., Arnold, L., Rasheed, A., Khan, I. A. & Wang, L. Textronics—A Review of Textile-Based Wearable Electronics. *Adv. Eng. Mater.* **2100469**, 1–19 (2021).
9. Fan, X. et al. Flexible and Wearable Power Sources for Next-Generation Wearable Electronics. *Batter. Supercaps* **3**, 1262–1274 (2020).
10. Islam, M. R., Afroj, S., Novoselov, K. S. & Karim, N. Smart Electronic Textile-Based Wearable Supercapacitors. *Adv. Sci.* **9**, 2203856 (2022).
11. Xiao, X. et al. Advances in solid-state fiber batteries for wearable bioelectronics. *Curr. Opin. Solid State Mater. Sci.* **26**, 101042 (2022).
12. Huang, Q., Wang, D. & Zheng, Z. Textile-Based Electrochemical Energy Storage Devices. *Adv. Energy Mater.* **6**, 1600783 (2016).
13. Noori, A., El-Kady, M. F., Rahmanifar, M. S., Kaner, R. B. & Mousavi, M. F. Towards establishing standard performance metrics for batteries, supercapacitors and beyond. *Chem. Soc. Rev.* **48**, 1272–1341 (2019).
14. Chen, S., Qiu, L. & Cheng, H.-M. Carbon-Based Fibers for Advanced Electrochemical Energy Storage Devices. *Chem. Rev.* **120**, 2811–2878 (2020).
15. Carvalho, J. T. et al. Carbon-Yarn-Based Supercapacitors with In Situ Regenerated Cellulose Hydrogel for Sustainable Wearable Electronics. *ACS Appl. Energy Mater* **5**, 11987–11996 (2022).
16. Borenstein, A. et al. Carbon-based composite materials for supercapacitor electrodes: A review. *J. Mater. Chem. A* **5**, 12653–12672 (2017).
17. Pomerantseva, E., Bonaccorso, F., Feng, X., Cui, Y. & Gogotsi, Y. Energy storage: The future enabled by nanomaterials. *Science (80-)* **366**, eaan8285 (2019).
18. Dai, H. et al. Polymer gel electrolytes for flexible supercapacitors: Recent progress, challenges, and perspectives. *Energy Storage Mater* **34**, 320–355 (2021).
19. Lei, Z., Zhan, J., Tang, L., Zhang, Y. & Wang, Y. Recent Development of Metallic (1T) Phase of Molybdenum Disulfide for Energy Conversion and Storage. *Adv. Energy Mater.* **8**, 1703482 (2018).
20. Jiao, Y. et al. Metallic MoS 2 for High Performance Energy Storage and Energy Conversion. *Small* **14**, 1800640 (2018).
21. Bello, I. T. et al. Molybdenum sulfide-based supercapacitors: From synthetic, bibliometric, and qualitative perspectives. *Int. J. Energy Res.* **45**, 12665–12692 (2021).
22. Sun, W. et al. Synthesis of MoS 2 -based nanostructures and their applications in rechargeable ion batteries, catalysts and gas sensors: a review. *RSC Adv.* **12**, 19512–19527 (2022).
23. Ishag, A. & Sun, Y. Recent Advances in Two-Dimensional MoS 2 Nanosheets for Environmental Application. *Ind. Eng. Chem. Res.* **60**, 8007–8026 (2021).
24. Rana, S., Singh, V. & Singh, B. Recent trends in 2D materials and their polymer composites for effectively harnessing mechanical energy. *iScience* **25**, 103748 (2022).
25. Yadav, V., Roy, S., Singh, P., Khan, Z. & Jaiswal, A. 2D MoS 2 -Based Nanomaterials for Therapeutic, Bioimaging, and Biosensing Applications. *Small* **15**, 1803706 (2019).
26. Upadhyay, K. K., Nguyen, T., Silva, T. M., Carmezim, M. J. & Montemor, M. F. Pseudocapacitive response of hydrothermally grown MoS2 crumpled nanosheet on carbon fiber. *Mater. Chem. Phys.* **216**, 413–420 (2018).
27. Shi, S., Sun, Z. & Hu, Y. H. Synthesis, stabilization and applications of 2-dimensional 1T metallic MoS 2. *J. Mater. Chem. A* **6**, 23932–23977 (2018).
28. Geng, X. et al. Two-Dimensional Water-Coupled Metallic MoS 2 with Nanochannels for Ultrafast Supercapacitors. *Nano Lett.* **17**, 1825–1832 (2017).
29. Rafique, A. et al. Binder Free and Flexible Asymmetric Supercapacitor Exploiting Mn3O4 and MoS2 Nanoflakes on Carbon Fibers. *Nanomaterials* **10**, 1084 (2020).
30. Thi Xuyen, N. & Ting, J.-M. Hybridized 1T/2H MoS2 Having Controlled 1T Concentrations and its use in Supercapacitors. *Chemistry* **23**, 17348–17355 (2017).
31. Tang, W. J. et al. Hollow metallic 1T MoS2 arrays grown on carbon cloth: A freestanding electrode for sodium ion batteries. *J. Mater. Chem. A* **6**, 18318–18324 (2018).
32. Shao, Y. et al. 3D Crumpled Ultrathin 1T MoS2for Inkjet Printing of Mg-Ion Asymmetric Micro-supercapacitors. *ACS Nano* **14**, 7308–7318 (2020).
33. Pan, H. et al. Assembly of 1T′-MoS 2 based fibers for flexible energy storage. *Nanoscale* **12**, 6562–6570 (2020).
34. Li, J. et al. 1T-Molybdenum disulfide/reduced graphene oxide hybrid fibers as high strength fibrous electrodes for wearable energy storage. *J. Mater. Chem. A* **7**, 3143–3149 (2019).
35. Zhao, W. et al. Metastable MoS2: Crystal Structure, Electronic Band Structure, Synthetic Approach and Intriguing Physical Properties. *Chemistry* **24**, 15942–15954 (2018).
36. Chodankar, N. R. et al. True Meaning of Pseudocapacitors and Their Performance Metrics: Asymmetric versus Hybrid Supercapacitors. *Small* **16**, 2002806 (2020).
37. Barras, R. et al. Porous PDMS conformable coating for high power output carbon fibers/ZnO nanorod-based triboelectric energy harvesters. *Nano Energy* **90**, 106582 (2021).

38. Isabel, A. et al. Hydrothermal Synthesis of Zinc Tin Oxide Nanostructures for Photocatalysis, Energy Harvesting and Electronics. *Nov. Nanomater*. https://doi.org/10.5772/INTECHOPEN.94294 (2020).
39. Serrapede, M. et al. A facile and green synthesis of a MoO2-Reduced graphene oxide aerogel for energy storage devices. *Materials (Basel)* **13**, 1–15 (2020).
40. Henriques Ferreira, S. et al. Porous ZnO Nanostructures Synthesized by Microwave Hydrothermal Method for Energy Harvesting Applications. in *Nanopores* 225–240 (IntechOpen, 2021). https://doi.org/10.5772/intechopen.97060.
41. Lee, C. M. et al. Effects of precursor concentration on morphology of MoS2 nanosheets by hydrothermal synthesis. *J. Nanosci. Nanotechnol.* **16**, 11548–11551 (2016).
42. Sahatiya, P., Jones, S. S. & Badhulika, S. Direct, large area growth of few-layered MoS 2 nanostructures on various flexible substrates: growth kinetics and its effect on photodetection studies. *Flex. Print. Electron.* **3**, 015002 (2018).
43. Zhou, C. et al. Vertical MoS2 nanosheets arrays on carbon cloth as binder-free and flexible electrode for high-performance all-solid-state symmetric supercapacitor. *Ceram. Int.* **45**, 21534–21543 (2019).
44. Sari, F. N. I. & Ting, J.-M. Direct Growth of MoS2 Nanowalls on Carbon Nanofibers for Use in Supercapacitor. *Sci. Rep.* **7**, 5999 (2017).
45. Xu, M., Reichman, B. & Wang, X. Modeling the effect of electrode thickness on the performance of lithium-ion batteries with experimental validation. *Energy* **186**, 115864 (2019).
46. Cordeiro, N. J. A. et al. Fast and Low-Cost Synthesis of MoS2 Nanostructures on Paper Substrates for Near-Infrared Photodetectors. *Appl. Sci.* **11**, 1234 (2021).
47. Abinaya, R. et al. Ultrathin layered MoS $_2$ nanosheets with rich active sites for enhanced visible light photocatalytic activity. *RSC Adv.* **8**, 26664–26675 (2018).
48. Fan, H. et al. Synthesis of metal-phase-assisted 1T@2H-MoS2 nanosheet-coated black TiO2 spheres with visible light photocatalytic activities. *J. Mater. Sci.* **53**, 10302–10312 (2018).
49. Radhakrishnan, S., Mane, P., Sree Raj, K. A., Chakraborty, B. & Rout, C. S. In-situ construction of hierarchical 2D MoS2/1D Te hybrid for supercapacitor applications. *J. Energy Storage* **60**, 106703 (2023).
50. Bissett, M. A., Kinloch, I. A. & Dryfe, R. A. W. Characterization of MoS 2 –Graphene Composites for High-Performance Coin Cell Supercapacitors. *ACS Appl. Mater. Interfaces* **7**, 17388–17398 (2015).
51. Wang, Z. et al. Hydrogel Electrolytes for Flexible Aqueous Energy Storage Devices. *Adv. Funct. Mater.* **28**, 1804560 (2018).

Acknowledgements

This work was financed by national funds from FCT - Fundação para a Ciência e a Tecnologia, I.P., in the scope of the projects LA/P/0037/2020, UIDP/50025/2020, and UIDB/50025/2020 of the Associate Laboratory Institute of Nanostructures, Nanomodelling and Nanofabrication – i3N, and projects 2022.04012.PTDC, and PTDC/CTM-PAM/4241/2020. J.T.C. acknowledges the support from the Portuguese Foundation for Science and Technology under the scholarship SFRH/BD/139225/2018, COVID/BD/153262/2023, and IDS-FunMat-INNO project FPA2016/EIT/EIT RawMaterials Grant Agreement 17184. João Coelho acknowledges the Portuguese Foundation for Science and Technology for funding under the Individual Call to Scientific Employment Stimulus program (ref. CEECIND/00880/2018). This work has received funding from the European Union's Horizon 2020 Research and Innovation Programme under Grant Agreements number, 952169 (SYNERGY, H2020-WIDESPREAD-2020-5, CSA), and 101008701 (EMERGE, H2020-INFRAIA-2020-1). The authors would also like to thank Daniela Gomes, Jonas Deuermeier, Maria João Oliveira, and Sofia Ferreira from CENIMAT|i3N for contributing to SEM, XPS, RAMAN, and XRD measurements, respectively. Carla Rodrigues and Nuno Costa for providing access to the Mettler Toledo AT21 Comparator microscale.

Author contributions

José Tiago Carvalho: Methodology, Investigation, Data Curation, Visualization, Writing – original draft. Afonso Correia: Methodology, Investigation, Curation, Writing – original draft. Neusmar J. A. Cordeiro: Methodology, Writing – Reviewing & Editing. João Coelho: Data Curation, Writing – reviewing & editing. Sidney A. Lourenço: Writing – Reviewing & Editing, Elvira Fortunato: Project administration, Funding acquisition. Rodrigo Martins: Writing – Reviewing & Editing, Supervision, Project administration, Funding acquisition. Luís Pereira: Conceptualization, Writing – Reviewing & Editing, Supervision, Project administration, Funding acquisition.

Competing interests

The authors declare no competing interests.

Additional information

Supplementary information The online version contains supplementary material available at https://doi.org/10.1038/s41699-024-00448-x.

Correspondence and requests for materials should be addressed to Luís. Pereira.